

nanodroplet water imbibed in poly(2-hydroxyethyl-methacrylate) (polyHEMA) near its glass transition at 162 K [the value given for a 34 wt % water sample (47, 48)]. These dielectric relaxation times are also Arrhenius in character and faster than the relaxation responsible for the glass transition.

The second is the convergence of extrapolated binary solution T_g to the temperature 138 ± 2 K (7, 11, 12). Here the resolution must be (7) the recognition that aqueous binary system extrapolations are no more reliable than those of binary solutions of other network-formers such as SiO_2 , BeF_2 , and ZnCl_2 . In such solutions there are sudden drops of T_g with small additions of the second component as the tetrahedral network is disrupted. In recent studies (49) of the $\text{BeF}_2 + \text{LiF}$ system, for instance, the binary solution T_g data measured by DSC between 4 and 10 mol % LiF predict, by extrapolation, that the T_g for pure BeF_2 should be 394 K. However, the directly measured value for pure BeF_2 glass is very much higher, 590 K, according to both DSC (49) and viscosity (50) measurements. Because there is general agreement that glassy water is well described as a random tetrahedral network (51), the BeF_2 system data should suffice to show that earlier uses of binary system extrapolations to obtain T_g for water (11, 12) were not correct.

In light of the new assignment, the glass transitions observed in hydrated proteins (52, 53) take on a new aspect. T_g values in these systems are observed to decrease rapidly with increasing water content until they reach ~ 165 K, and then excess water crystallizes out as ice during cooling. Water in association with hydrophilic proteins behaves much like water in hydrogels (54). Both cases may reflect the behavior of water in the absence of crystallization.

Vitreous water, like most hyperquenched metallic glasses, apparently remains in the glassy state until it crystallizes (at 150 to 160 K). A possible exception is water sequestered in nanoscopic assemblages, which may play an important role in biophysical systems.

References and Notes

1. P. Jenniskens, S. F. Barnhak, D. F. Blake, M. R. S. McCoustra, *J. Chem. Phys.* **107**, 1232 (1997).
2. M. G. Sceats, S. A. Rice, in *Water: A Comprehensive Treatise*, F. Franks, Ed. (Plenum, London, 1982), vol. 7, pp. 83–211.
3. E. F. Burton, W. F. Oliver, *Nature* **135**, 505 (1935).
4. ———, *Proc. R. Soc. London Ser. A* **153**, 166 (1935).
5. C. A. Angell, *Science* **267**, 1924 (1995).
6. J. A. Pryde, G. O. Jones, *Nature* **170**, 635 (1952).
7. D. R. MacFarlane, C. A. Angell, *J. Phys. Chem.* **88**, 759 (1984).
8. J. A. Ghormley, *J. Chem. Phys.* **48**, 503 (1967).
9. J. A. MacMillan, S. C. Los, *J. Chem. Phys.* **42**, 829 (1965).
10. M. Sugisaki, H. Suga, S. Seki, *J. Chem. Soc. Jpn.* **41**, 2591 (1968).
11. C. A. Angell, J. C. Tucker, *J. Phys. Chem.* **84**, 268 (1980).
12. J. A. Ghormley, *J. Am. Chem. Soc.* **79**, 1862 (1957).
13. A. Hallbrucker, E. Mayer, G. P. Johari, *J. Phys. Chem.* **93**, 4986 (1989).

14. G. P. Johari, A. Hallbrucker, E. Mayer, *Nature* **330**, 552 (1987).
15. E. Mayer, *J. Appl. Phys.* **58**, 663 (1985).
16. ———, *J. Microsc.* **140**, 3 (1985).
17. O. Mishima, L. D. Calvert, E. Whalley, *Nature* **314**, 76 (1985).
18. D. D. Klug, Y. P. Handa, *J. Phys. Chem.* **92**, 3323 (1988).
19. A. Hallbrucker, E. Mayer, G. P. Johari, *J. Phys. Chem.* **93**, 7751 (1989).
20. G. P. Johari, A. Hallbrucker, E. Mayer, *Science* **273**, 90 (1996).
21. G. P. Johari, *J. Phys. Chem. B* **102**, 4711 (1998).
22. K. Ito, C. T. Moynihan, C. A. Angell, *Nature* **398**, 492 (1999).
23. O. Mishima, H. E. Stanley, *Nature* **396**, 329 (1998).
24. A. A. Tsekouras, M. J. Ledema, J. P. Cowin, *Phys. Rev. Lett.* **80**, 5798 (1998).
25. ———, in preparation.
26. M. Fisher, J. P. Devlin, *J. Phys. Chem.* **99**, 11584 (1995).
27. A. Hallbrucker, E. Mayer, *J. Phys. Chem.* **91**, 503 (1987).
28. C. T. Moynihan, A. J. Easteal, M. A. DeBolt, J. Tucker, *J. Am. Ceram. Soc.* **59**, 12 (1976).
29. ———, *J. Am. Ceram. Soc.* **59**, 16 (1976).
30. G. W. Scherer, *Relaxation in Glass and Composites* (Wiley, New York, 1986).
31. J. Huang, P. K. Gupta, *J. Non-Cryst. Solids* **151**, 175 (1992).
32. Y. Yue, in preparation. This study is of a nonstandard basalt glass, but is very detailed.
33. I. M. Hodge, *J. Non-Cryst. Solids* **169**, 211 (1994).
34. G. Adam, J. H. Gibbs, *J. Chem. Phys.* **43**, 139 (1965).
35. C. T. Moynihan, P. B. Macedo, *J. Phys. Chem.* **75**, 3379 (1971).
36. R. Bohmer, K. L. Ngai, C. A. Angell, D. J. Plazek, *J. Chem. Phys.* **99**, 4201 (1993).

37. W. T. Laughlin, D. R. Uhlmann, *J. Phys. Chem.* **76**, 2317 (1972).
38. V. Velikov, S. Borick, C. A. Angell, *J. Phys. Chem.*, in press.
39. H. S. Chen, E. Coleman, *Appl. Phys. Lett.* **28**, 245 (1976).
40. J. Doshi, D. H. Reneker, *J. Electrostat.* **35**, 151 (1995).
41. D. H. Reneker, I. Chun, *Nanotechnology* **7**, 216 (1996).
42. R. S. Smith, B. D. Kay, *Nature* **398**, 788 (1999).
43. D. H. Reneker, G. Tarjus, *J. Phys. Chem. B* **105**, 6620 (2001).
44. E. Mayer, personal communication.
45. C. Meingast, F. Gugenberger, *Mod. Phys. Lett. B* **7**, 1703 (1993).
46. F. Starr, C. A. Angell, H. E. Stanley, in preparation.
47. K. Hofer, E. Mayer, G. P. Johari, *J. Phys. Chem.* **94**, 2689 (1990).
48. ———, *J. Phys. Chem.* **95**, 7100 (1991).
49. Zh. V. Dobrokhotova, B. S. Zakharova, *Inorg. Mater.* **36**, 191 (2000) (translated from the Russian original).
50. S. V. Nemilov, G. T. Petrovskii, L. A. Krylova, *Inorg. Mater.* **4**, 1453 (1968).
51. A. H. Narten, C. G. Venkatesh, S. A. Rice, *J. Chem. Phys.* **64**, 1106 (1976).
52. G. Sartor, E. Mayer, G. P. Johari, *Biophys. J.* **66**, 249 (1994).
53. J. L. Green, J. Fan, C. A. Angell, *J. Phys. Chem.* **98**, 13780 (1994).
54. G. Sartor, A. Hallbrucker, E. Mayer, *Biophys. J.* **69**, 2679 (1995).
55. R. J. Speedy, unpublished data.
56. Supported by NSF Solid State Chemistry Program grants DMR-9614531 and DMR-0082535. We acknowledge R. J. Speedy (55), who argued, using data from some of the same references cited here, that T_g should lie far above 136 K, perhaps near 220 K. We thank E. Mayer for sharing unpublished data.

19 April 2001; accepted 26 October 2001

High Geothermal Heat Flow, Basal Melt, and the Origin of Rapid Ice Flow in Central Greenland

Mark Fahnestock,¹ Waleed Abdalati,² Ian Joughin,³ John Brozena,⁴ Prasad Gogineni⁵

Age-depth relations from internal layering reveal a large region of rapid basal melting in Greenland. Melt is localized at the onset of rapid ice flow in the large ice stream that drains north off the summit dome and other areas in the northeast quadrant of the ice sheet. Locally, high melt rates indicate geothermal fluxes 15 to 30 times continental background. The southern limit of melt coincides with magnetic anomalies and topography that suggest a volcanic origin.

Basal melt and meltwater exert a strong influence on ice flow (1–4). Our limited knowledge of basal melt is derived from models and sparse observations of bed properties (5–

7). Here we introduce a technique that allows us to determine the extent and rate of basal melting for a large portion of the Greenland Ice Sheet using data from airborne ice-penetrating radar, and we relate that melting to ice flow patterns in the interior.

Radar soundings reveal internal layering (8–11) largely due to changes in electrical conductivity from inhomogeneous impurity concentrations within the ice. The impurities (e.g., dust from volcanic eruptions) are introduced from the atmosphere, forming layers

¹Earth System Science Interdisciplinary Center, University of Maryland, College Park, MD 20742, USA. ²NASA Headquarters, Washington, DC 20546, USA. ³Jet Propulsion Laboratory, Mail Stop 300-235, 4800 Oak Grove Drive, Pasadena, CA 91109, USA. ⁴Naval Research Laboratory, Washington, DC 20375, USA. ⁵Remote Sensing Laboratory, University of Kansas, Lawrence, KS 66045, USA.

REPORTS

that represent constant time horizons across the ice sheet. Advances in radar sounders, satellite-based navigation, and the dating of the deep ice cores in central Greenland (12–14) have improved our ability to interpret the accumulation and flow histories recorded by this layering.

Fahnestock and others (15) have traced numerous internal layers along a single flight track flown by a NASA P-3 Aircraft carrying a University of Kansas ice-penetrating radar (9) and a NASA laser altimeter (16). The flight passed over ice core sites in central Greenland so that layers could be dated and an age-versus-depth relation could be established. Through layer tracing, this relation is extended along the entire flight line. The long-term [~ 8 thousand years (ky)] accumulation rate can be estimated by fitting a simple model of ice flow, which earlier studies used to determine the age-depth function for ice cores, to the data. Here this analysis is extended to additional flight lines and is modified to deal with anomalous layering patterns and age-depth relations that occur at several locations. Although the disturbances in internal layering appear complicated, they can be explained with a simple addition to the technique of Fahnestock and others that incorporates basal melting.

In a steady state ice sheet, the age-depth relation is determined by the balance between

surface accumulation of snow and thinning of ice due to horizontal gradients in flow speed. Simple models that estimate vertical strain rates using surface accumulation estimates and ice thickness are used to provide provisional timescales for paleoclimate records in ice cores. Nye (17) proposed a model using a constant vertical strain rate to balance local accumulation. The vertical strain rate, $\dot{\epsilon}_{\text{Nye}}$, is equal to the ice-equivalent accumulation rate, λ_H , divided by ice thickness H [notation follows Dansgaard and Johnsen (18)]: $\dot{\epsilon}_{\text{Nye}} = \lambda_H/H$. A constant strain rate with depth implies that the thinning is produced by gradients in sliding velocity at the bed, with a vertical column of ice remaining vertical through the deformation. Dansgaard and Johnsen (18) proposed a more complex model, based on a fit of two linear functions to variations in horizontal ice flow speed with depth, which produces better results in areas where the ice is frozen to the bed. In this model, the ice above a basal shearing section deforms in the same way as the Nye model (constant strain rate with depth) at a maximum strain rate $\dot{\epsilon} = \dot{\epsilon}_{\text{D-J}}$. In the shearing section (below a height h above the bed), the vertical strain rate drops off linearly to zero to accommodate the no-slip boundary condition: $\dot{\epsilon} = (z/h) \dot{\epsilon}_{\text{D-J}}$ ($0 \leq z \leq h$, where z is the vertical coordinate measured upward from the bed). The models are equivalent when

$h = 0$ (basal sliding); the Dansgaard-Johnsen model with $h > 0$ produces a more rapid increase in ice age with depth near the surface than does the Nye model, resulting in older ice higher in the column (19).

In ice-penetrating radar records from Greenland, there are areas where the Dansgaard-Johnsen and Nye models do not fit the age-depth relations from internal layer tracing. In these areas, a simple modification to the continuum represented by these models produces an acceptable fit. We modify the

Fig. 1. Accumulation rate for the interior of the Greenland Ice Sheet, derived from fitting internal layers younger than 9000 years, plotted over the surface topography of the ice sheet (39). The accumulation rate is used to determine both the color and the size of the plotted filled circles. The data have not been smoothed. This long-term accumulation rate should be the best available for driving ice-flow models that are attempting to simulate present conditions for this part of the ice sheet. The topographic control on accumulation is clearly evident, as discussed in the text. Boxes locate the areas shown in Figs. 2 and 4.

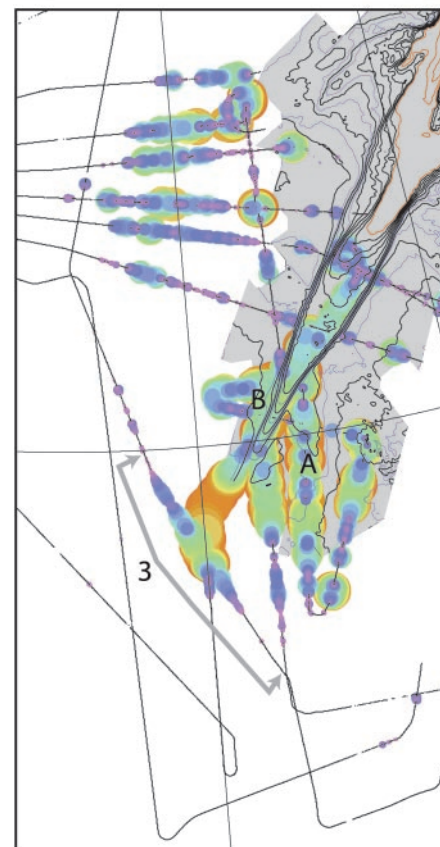
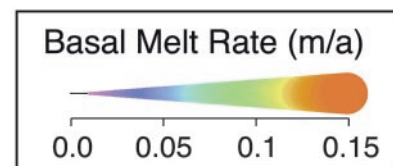
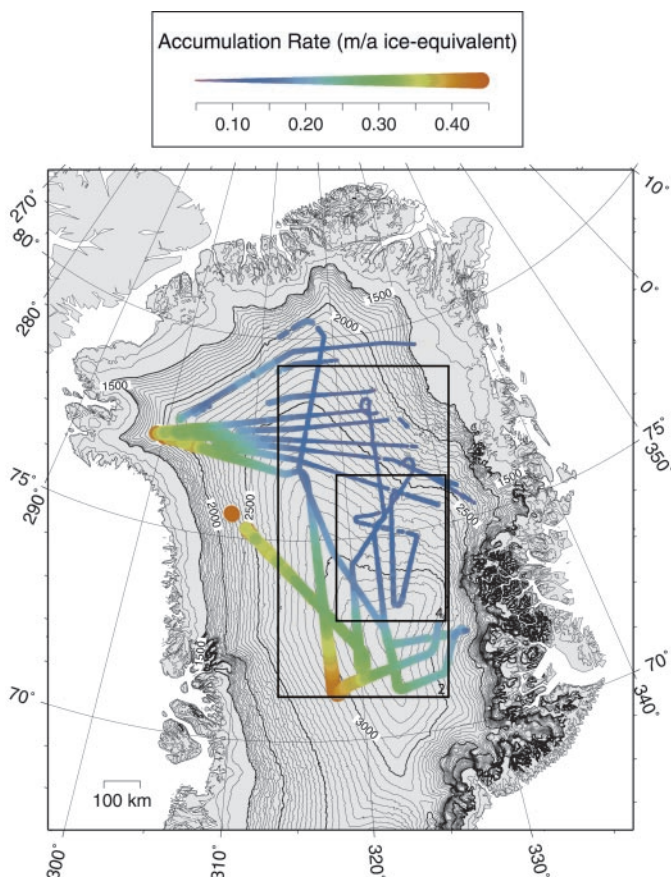


Fig. 2. Basal melt rate and rapid ice flow. Basal melt rate along the flight lines shown in Fig. 1. The color and size of the circles plotted along flight are both a function of the basal melt rate. Nonmelting areas and areas where the melt rate is < 1 cm/a of ice are shown as thin black lines. The region of high basal melt rates corresponds spatially with the onset of rapid ice flow measured by interferometric techniques. Interferometric ice flow speed data are available in the grey regions, which depict ERS SAR satellite coverage. The black speed contours have a 10 m/a interval from 10 to 90 m/a; the blue contours cover 5, 15, 25, 35, and 45 m/a; and the red contours have a 100 m/a interval starting at 100 m/a. The segment of flight shown in Fig. 3 is indicated by the gray arrows.

Nye model to accommodate excess heat at the bed by allowing melting of basal ice (20). The vertical strain rate in steady state will be less than $\dot{\epsilon}_{Nye}$ because the ice lost at the bed reduces the need to thin the ice by flow. The new vertical strain rate $\dot{\epsilon}_{melt}$ is equal to the difference between the surface accumulation rate and the basal melt rate (\dot{m}) divided by the ice thickness (21)

$$\dot{\epsilon}_{melt} = \frac{\lambda_H - \dot{m}}{H} = \dot{\epsilon}_{Nye} - \frac{\dot{m}}{H} \quad (1)$$

In this model, an annual layer of ice will thin more slowly with depth than in either the Dansgaard-Johnsen or Nye models (22). Because of melting, the predicted age of ice at the bed is no longer infinite, as is the case in the other approaches.

We have traced internal layers, dated at ice core sites, within and between flight lines over the dry snow zone of the Greenland Ice Sheet using methods previously described (15). We performed inversions to determine best-fit accumulation rate and shear layer thickness for a Dansgaard-Johnsen age-depth model. This was accomplished with the use of a two-dimensional minimization of misfit between the function $f(\lambda_H, h)$ and the dated layers in a radar profile with ages t_i and depths d_i (23). The fits were performed using only layers younger than 9000 years, chosen to coincide with the most recent interval when accumulation in central Greenland was nearly constant (14, 24, 25).

In areas where internal layering appeared disturbed, the minimization returned a negative value for h . This nonphysical result indicates that the thinning observed is slower than would be required to balance accumulation. In locations where the initial fit returned $h < 0$, the misfit for the Dansgaard-Johnsen model was recalculated with $h = 0$ (basal sliding case) and the modified Nye model was constrained with a misfit function $f(\lambda_H, \dot{m})$, providing estimates of accumulation rate and basal melt rate (26). In all cases where the Dansgaard-Johnsen model initially indicated $h < 0$, the modified Nye model yielded an improved fit to the observed age-depth pairs.

The pattern of ~8 ky average accumulation rate (Fig. 1) determined from this set of techniques shows large gradients across flow divides, indicating that orographic controls on precipitation are strong. Movement of air masses up from the west leads to high accumulation along this coast, whereas the descent of these air masses just past the ice divide limits accumulation in the northeast quadrant of the ice sheet. The spatial coherence of the accumulation signal demonstrates the effectiveness of the techniques we have used (27).

A map of basal melt rate along the same

flight tracks (Fig. 2) shows no melt in many areas (thin black lines) and very high rates of melting on the northern flank of the summit dome. The high melt rates coincide with the disturbed topography (Fig. 2) associated with rapid flow that begins in this region (28, 29). Much of the low-accumulation northeastern quadrant of the ice sheet shows more limited melting at the bed. This is consistent with theory because the temperature gradient in the basal ice is lower in low-accumulation regions due to lowered rates of downward advection of cold ice, allowing the bed to be warmed to the melting point by geothermal heat (30).

Disturbance to internal layering caused by basal melting is visible in individual radar profiles (Fig. 3). The radar data re-mapped onto an age axis (Fig. 3) show the success of the model fits and the self-similarity of the layering along flight. The thinning rate experienced by the upper layers is higher than would be produced by sliding on the left end of the profile, but in the right half of the figure there are areas where the basal melt rate approaches the surface accumulation rate

and the thinning rate approaches zero. Flow in these areas produces no net thinning of the ice, which is lost only to melting. The shear layer thickness h drops off as melt areas are approached. Low values of h are observed to coincide with visible disturbance of internal layers near the bed; the disturbance becomes more pronounced and affects layers farther up in the column as melt (and sliding) begins.

A basal melt rate of 0.1 m/a over a substantial area requires a regional geothermal heat flux of 970 mW m⁻², which is 17 times higher than the continental background of 56.5 mW m⁻² (31). This does not account for heat conducted through the ice. For most of the ice sheet, the heat conducted through the ice is close to the background geothermal heat flux. It can be lower in low-accumulation regions because the thermal gradient in the basal ice is lower. The volume of meltwater being produced in the areas of high basal melt is of the order of one cubic kilometer per year. This water and warm basal ice are responsible for the onset of rapid ice flow in the large ice stream that drains the north side of the summit dome. The locations of

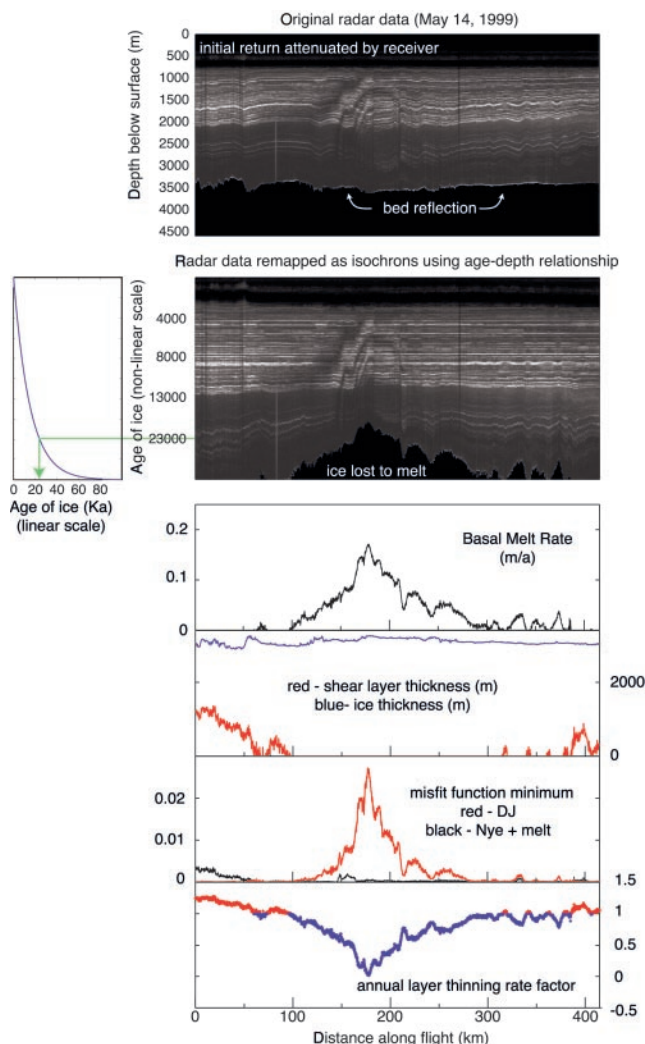


Fig. 3. Northwest ridge radar profiles, and the same data mapped versus a "standard" age-depth function using the derived age-depth function at each profile. The horizontal character of the layers mapped by age shows the effectiveness of the layer tracing and model fits; the self-similarity of the layer patterns along the radar profiles displayed in this manner demonstrates their isochronous nature. The quantities plotted include the derived basal melt rate, ice thickness H and shear layer thickness h , misfit function values for both the Dansgaard-Johnsen and Nye-with-melt models, and the thinning rate factor f .

rapid basal melting correspond well with the onset of rapid ice flow (Fig. 2). The contoured ice flow speeds are measured using interferometric techniques (28). Comparison of maps of basal melt rate and topography suggests that the ice stream has its origins directly under the ice divide, at the break in slope along the northwest ridge. This break in slope, with no corresponding change in bed topography, can now be interpreted as the place where extending ice flow along the ridge slows down as thinning rates drop in response to rapid basal melting. The initial sliding of the ice over its bed occurs in this area. The “southern tributary” (marked “A” in Fig. 2) discussed by Joughin and others (28) and Fahnestock and others (29) has its origins in basal melting as well. In addition, the step-out of the northwestern margin of the ice stream at the start of the wedge-shaped section is related to an increase in basal melt rate (location “B” in Fig. 2).

The region of rapid basal melting corresponds closely (Fig. 4) with a low in the free-air gravity measured as part of the Greenland Aerogeophysics Program (GAP) (32–34). At the southern limit of rapid basal melt, there is a gravity high, a local strong normally magnetized area (32), and a coincident topographic edifice in the bed (“M” in Fig. 4). Radio-echo sounding reveals a

1000-m topographic high that shows a dramatic increase in bed roughness, suggesting it has undergone less erosion and may be younger than the surrounding bed. We cannot be certain of the presence of volcanic features; however, the mass deficit in the gravity and the corresponding area of high conductive heat flux are comparable in magnitude and spatial extent to the Yellowstone caldera (35), and the localized peaks in gravity and rough-surfaced bed topography suggest local extrusive structures.

We use models that assume a local steady state, implying that the ice at a point is neither thickening nor thinning and that the accumulation rate and basal melt rate are constant over the interval considered. Before the last 9000 years, accumulation rates were substantially lower (14, 24, 25). The ice sheet thickness should respond to the increase with a characteristic time of the order of several millennia (30), thickening rapidly at first in response to the increase in accumulation rate, but then more slowly as the ice flow adjusted (36).

Present measurements of thickening and thinning in the high interior of the ice sheet indicate stability at the few-centimeter-per-year level (16, 37, 38). Perhaps more important is the fact that these measurements do not show large gradients in thickness changes on

the 100-km scale of our determinations of basal melting. Rather, they show only longer wavelength variations of small amplitude. This suggests the present ice sheet is close to being in balance with the patterns of basal melting that we present here.

We assume that the basal melt rate is constant over the interval considered. We do not include the possibility that some of the heating is a more recent phenomenon. If the melt was initiated only a few hundred years ago, the initial age-depth relation would have reflected a more rapid thinning rate based on the Dansgaard-Johnsen model. It would be this age-depth relation that would be the starting point for the slower thinning under a Nye-with-melt regime. This would result in a best-fit solution that would under-predict the actual melt rate.

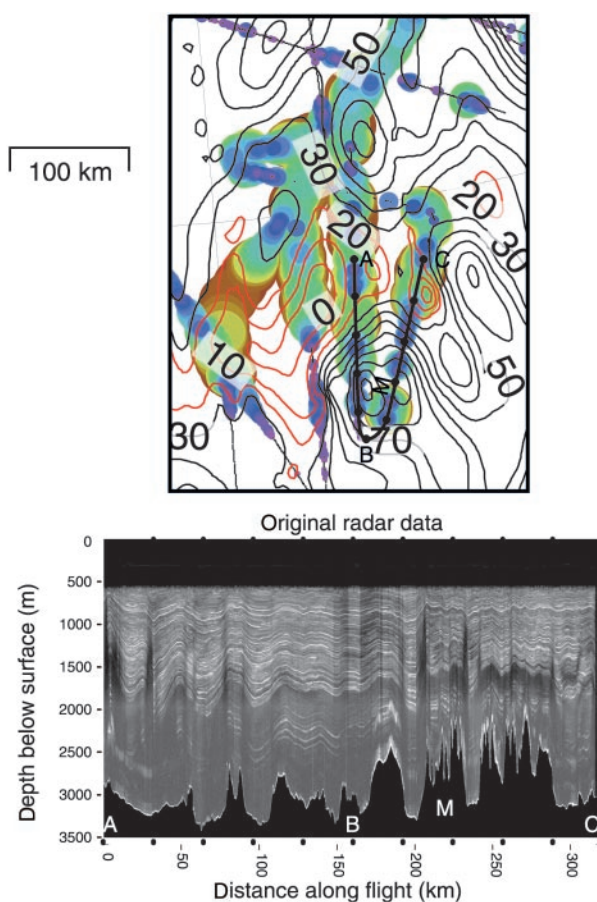
Within these limits, we have identified rapid and extensive basal melting in Greenland that has a direct effect on ice flow. The source of the high heat flow is not well constrained, but limited geophysical evidence suggests the presence of a caldera structure.

References and Notes

1. S. Tulaczyk, W. B. Kamb, H. F. Engelhardt, *J. Geophys. Res.* **105**, 483 (2000).
2. A. C. Fowler, C. Johnson, *J. Glaciol.* **41**, 554 (1995).
3. C. F. Raymond, *J. Glaciol.* **46**, 665 (2000).
4. D. D. Blankenship *et al.*, *Nature* **361**, 526 (1993).
5. H. Engelhardt, B. Kamb, *J. Glaciol.* **43**, 207 (1997).
6. C. L. Hulbe, D. R. MacAyeal, *J. Geophys. Res.* **104**, 25349 (1999).
7. P. Huybrechts, J. de Wolde, *J. Climate* **12**, 2169 (1999).
8. R. W. Jacobel, S. M. Hodge, *Geophys. Res. Lett.* **22**, 587 (1995).
9. S. Gogineni, T. Chuah, C. Allen, K. Jezek, R. K. Moore, *J. Glaciol.* **44**, 659 (1998).
10. L. Hempel, F. Thyssen, N. Gundestrup, H. B. Clausen, H. Miller, *J. Glaciol.* **46**, 369 (2000).
11. K. C. Taylor *et al.*, *Nature* **366**, 549 (1993).
12. S. J. Johnsen *et al.*, *J. Geophys. Res.* **102**, 26397 (1997).
13. D. A. Meese *et al.*, *J. Geophys. Res.* **102**, 26411 (1997).
14. R. B. Alley *et al.*, *J. Geophys. Res.* **102**, 26367 (1997).
15. M. Fahnestock, W. Abdalati, S. Luo, S. Gogineni, *J. Geophys. Res.*, in press.
16. W. Krabill *et al.*, *Science* **289**, 428 (2000).
17. J. F. Nye, *Proc. R. Soc. London Ser. A* **239**, 113 (1957).
18. W. Dansgaard, S. J. Johnsen, *J. Glaciol.* **8**, 215 (1969).
19. The average thinning rate in the shearing section is half the rate above the height h , requiring $\dot{\epsilon}_{D-J}$ to be greater than $\dot{\epsilon}_{Nye}$ to balance local accumulation. The relation between the thinning rates in the Dansgaard-Johnsen model and the Nye model is

$$\dot{\epsilon}_{D-J} = \frac{\dot{\epsilon}_{Nye}}{\left(1 - \frac{\alpha}{2}\right)}, \alpha = \frac{h}{H}$$
20. The continuum covered by the two models spans the range of ice flow situations from thinning due to internal deformation in ice frozen to the bed (the Dansgaard-Johnsen model with $h > 0$) to thinning due to gradients in basal sliding (the Nye model, or Dansgaard-Johnsen with $h = 0$). The addition of a basal melt rate term to the Nye model is motivated by the likelihood of basal sliding dominating motion in ice that is melting at the bed.
21. The Nye model modified to allow for basal melt gives a timescale expressed as

Fig. 4. Relation between airborne gravity measurements and basal melt rate. Contour interval 10 mgal, (red \leq 20 mgal, black \geq 30 mgal). Note the strong correspondence between the 30 to 50 mgal low in the free-air gravity data and the area of rapid basal melting. The bottom plot is the radar profile along the (A-B-C) black section of flight line (round black distance marks), which crosses several GAP flights. The radar profile shows several mountains that rise abruptly from the bed in this area; most notably the one labeled M (located at the gravity high in the area) and the next edifice to the north. Both of these features show rougher bed topography than anything else observed along this or most of the other profiles. This suggests a poorly eroded feature that is likely younger than its surroundings.



$$t_m(z) = -\frac{H}{\lambda_H - \dot{m}} \ln \left(\frac{1 - \frac{\dot{m}}{\lambda_H} z + \frac{\dot{m}}{\lambda_H}}{H - z + \frac{\dot{m}}{\lambda_H}} \right)$$

where t_m is the model age of ice at a depth $d = (H - z)$.

22. If the melt rate exceeds the surface accumulation rate, the thickness of an annual layer actually increases with age and depth in the ice (which is equivalent to saying that there is net convergence of flow in the horizontal plane or a slow-down along flow in a flow-line model). This situation occurs in several areas in northeast Greenland. The thinning rate can be expressed with a thinning rate factor

$$f = \frac{\dot{\epsilon}_{D-J}}{\dot{\epsilon}_{Nye}}, h > 0; f = \frac{\dot{\epsilon}_{melt}}{\dot{\epsilon}_{Nye}} = 1 - \frac{\dot{m}}{\lambda_H}, h = 0$$

which is the ratio of the strain rate required by the best-fit age-depth relation divided by the Nye strain rate. It is greater than 1 for a Dansgaard-Johnsen fit, and less than 1 for a Nye-with-melting fit.

23. The details of this fit are covered in Fahnestock and others (15). The misfit function is

$$f(\lambda_H, \dot{m}) = \sum_{i=1}^n \left[\frac{t_m(\lambda_H, \dot{m}, d(i)) - t(i)}{t(i)} \right]^2$$

24. D. Dahl-Jensen, S. J. Johnsen, C. U. Hammer, H. B. Clausen, J. Jouzel, in *Ice in the Climate System*, W. R. Peltier, Ed. (Springer-Verlag, Berlin, 1993), vol. 1(12), pp. 517–532.
 25. K. M. Cuffey, G. D. Clow, *J. Geophys. Res.* **102**, 26383 (1997).
 26. The misfit function for the Nye model modified to allow melting is

$$f(\lambda_H, \dot{m}) = \sum_{i=1}^n \left[\frac{t_m(\lambda_H, \dot{m}, d(i)) - t(i)}{t(i)} \right]^2$$

The modified Nye model returned a more smoothly varying estimate of accumulation rate along the flight in the areas where the Dansgaard-Johnsen model returned $h < 0$.

27. The spatial variations in accumulation patterns compare well with patterns determined from shallow firn cores and snow pits by the NASA PARCA program and earlier work.
 28. I. R. Joughin, M. A. Fahnestock, J. L. Bamber, *Ann. Glaciol.* **31**, 141 (2000).
 29. M. A. Fahnestock et al., *J. Geophys. Res.*, in press.
 30. W. S. B. Paterson, *The Physics of Glaciers* (Elsevier Science Ltd., Oxford, ed. 3, 1994), pp. 215–235 and 318–354.
 31. J. G. Sclater, C. Jaupart, D. Galson, *Rev. Geophys.* **18**, 269 (1980).
 32. J. M. Brozena, thesis, University of Cambridge (1996).
 33. ———, *The Greenland Aerogeophysics Project: Airborne Gravity, Topographic and Magnetic Mapping of an Entire Continent*, IAG Symposium No. 110, 20 August 1991, Vienna, Austria (Springer-Verlag, New York, 1991), pp. 203–214.
 34. J. Brozena, M. Chalona, R. Forsberg, G. Mader, *Eos* **74**, 18 (1993).
 35. R. B. Smith, L. W. Braile, *J. Volcanol. Geotherm. Res.* **61**, 121 (1994).
 36. Modeled results from the GISP2 core suggest that the accumulation rate has only been slowly increasing over the last 9000 years. This result, barring a change in average storm tracks, may well be applicable to other parts of the inland ice. The assumption that the ice thickness has been constant over this interval is perhaps less well supported by the available data. A rapid increase in ice thickness (at approximately half the accumulation rate) would produce an age-depth relation in the upper (younger) layers that showed slower than expected thinning rates. This would translate into an estimate that included basal melting using our technique. However, this would predict a basal melt rate that was essentially the same as the thickening rate. The basal melting we identify is larger than any measured thickening, and the spatial patterns of melting and thickening do not match.

37. C. H. Davis, C. A. Kluever, B. J. Haines, *Science* **279**, 2086 (1998).
 38. H. J. Zwally, M. B. Giovinetto, *Ann. Glaciol.* **31**, 126 (2000).
 39. T. A. Scambos, M. A. Fahnestock, *J. Glaciol.* **44**, 97 (1998).
 40. Supported by NASA Headquarters Program for Arctic

Regional Climate Assessment (PARCA) (M.F., W.A., I.J., and P.G.). Analysis of the airborne gravity and magnetic data (J.B.) were supported under Program Element 61153N of the ONR 6.1 program. We thank C. Shuman, T. Scambos, and two anonymous reviewers for reviewing the manuscript.

14 August 2001; accepted 25 October 2001

A New Global Mode of Earth Deformation: Seasonal Cycle Detected

Geoffrey Blewitt,^{1,2*} David Lavallée,¹ Peter Clarke,² Konstantin Nurutdinov²

We have detected a global mode of Earth deformation that is predicted by theory. Precise positioning of Global Positioning System sites distributed worldwide reveals that during February to March, the Northern Hemisphere compresses (and the Southern Hemisphere expands), such that sites near the North Pole move downward by 3.0 millimeters, and sites near the equator are pulled northward by 1.5 millimeters. The opposite pattern of deformation occurs during August to September. We identify this pattern as the degree-one spherical harmonic response of an elastic Earth to increased winter loading of soil moisture, snow cover, and atmosphere. Data inversion shows the load moment's trajectory as a great circle traversing the continents, peaking at 6.9×10^{22} kilogram meters near the North Pole in winter, indicating interhemispheric mass exchange of $1.0 \times 10^{16} \pm 0.2 \times 10^{16}$ kilograms.

Redistribution of mass over Earth's surface generates changes in gravitational and surface forces that produce a stress response in the solid Earth, accompanied by characteristic patterns of surface deformation (1–3). Here, we search for global deformation resulting from Earth's elastic response to a change in the “load moment” (a dipole moment), defined as the load center of mass vector multiplied by the load mass. This predicted degree-one spherical harmonic mode (1, 4) has unique characteristics that distinguish it from tidal deformation. Our calculations predict that the known seasonal exchange of water and air between the Northern and Southern hemispheres (5–7) is of sufficient magnitude to force such a mode with annual period at the several-millimeter level, which ought to be detectable by modern geodetic techniques. Monitoring this mode should enable global characterization of the hydrological cycle through direct inversion of geodetic data, and enable determination of mechanical properties of Earth on the global scale.

Previous investigations in space-based geodesy have detected displacements of surface

height at the 10-mm level in response to variation in atmospheric pressure (8) and large-scale terrestrial water storage (9). Such results show statistically significant correlation between observed site position variations and model predictions. Although promising, the residual discrepancies between data and models remain at least as large as the predicted signal. Apart from current uncertainties in modeling groundwater storage, another limitation is the level of noise in globally referenced site position data (9). We mitigate these problems by seeking a deformation mode with a theoretical functional form (allowing for inversion) and large-scale spatio-temporal coherence (enhancing the signal-to-noise ratio).

The change in Earth's shape due to the gravitational and pressure stresses of surface loading is theoretically characterized by spherical harmonic potential perturbations and load Love numbers (2). Load Love number theory is fundamental to the Green's function approach to loading models (1), which has facilitated numerical computation of Earth deformation due to arbitrary load distributions (3). Unlike tidal theory, loading theory includes a degree-one deformation generated by movement of the load center of mass with respect to the solid Earth center of mass (1, 4, 10).

Let us define CM as the center of mass of the solid Earth plus the load, and CE as the center of mass of the solid Earth only. CM

¹Nevada Bureau of Mines and Geology, and Seismological Laboratory, University of Nevada, Reno, NV 89557, USA. ²Department of Geomatics, University of Newcastle, Newcastle upon Tyne, NE1 7RU, UK.

*To whom correspondence should be addressed. E-mail: gblewitt@unr.edu